Catalysis Today 387 (2022) 159–171

Contents lists available at ScienceDirect

Catalysis Today

journal homepage: www.elsevier.com/locate/cattod

Nature and identity of the active site via structure-dependent microkinetic modeling: An application to WGS and reverse WGS reactions on Rh

Raffaele Cheula, Matteo Maestri *

Laboratory of Catalysis and Catalytic Processes, Dipartimento di Energia, Politecnico di Milano, Via La Masa, 34, 20156, Milano, Italy

ARTICLE INFO

Keywords:
WGS and reverse WGS on Rh
First-principles microkinetic modeling
Active site
Wulff construction
Ab initio thermodynamics
Catalyst structure

ABSTRACT

We propose a methodology to perform a structure-dependent microkinetic analysis of a catalytic process. The methodology makes it possible to unveil the *nature* and *identity* of the active site in a self-consistent manner. The morphology of heterogeneous catalyst nanoparticles as a function of the gas chemical potential is determined using *ab initio* thermodynamics and Wulff-Kaishew construction methods. The reaction rates are calculated by integrating a microkinetic model which describes the catalytic activity of the crystal facets exposed by the catalyst under reaction conditions. The method is applied for the analysis of the direct and reverse water-gas shift (WGS) reacting systems on a 4% Rh/α-Al_2O_3 kinetic experiments from the literature. Our findings make it possible to rationalize that far from equilibrium the two different reacting systems not only follow different reaction pathways in agreement with the experimental evidence but also show that the dominant active sites are different for WGS and reverse WGS. Indeed, the WGS reaction occurs mainly on the Rh(111) facet, whereas reverse WGS proceeds on the active sites of Rh(100). As a whole, this methodology makes it possible a concomitant description of the nature of the catalyst material in reaction conditions and of its catalytic consequences in terms of reactivity. As such, it paves the way towards the use of first-principles methods for the interpretation of the experimental evidence in terms of structure-activity relationships.

1. Introduction

The application of first-principles methods in catalysis is crucial for the rational understanding of catalysts' functionality with an atomistic level of detail [1–4]. On the one side, the possibility of modeling the surface chemistry at the fundamental level makes it possible to predict the catalytic process under different operating conditions, thus paving the way to catalyst design and process intensification [5]. On the other side, the application of these methods is limited by two main important challenges that need to be overcome especially for processes and operating conditions of technological and industrial interest [6]. The first one is related to the fact that we are dealing with "*imperfect theories*", i.e., insufficient accuracy of the solution of the quantum mechanical problem (e.g., type of exchange and correlation functional for the solution of the density functional theory problem). The second one concerns the fact that we are dealing also with "*imperfect models*" of the catalyst. First-principles methods intrinsically require the knowledge of the catalyst structure in reaction conditions. The atoms at the catalyst surface are arranged in diverse geometric configurations, providing numerous types of active sites, i.e., the centers for adsorption and subsequent reaction of chemical species [7–10]. In particular, supported catalyst nanoparticles expose to the reaction environment different crystal facets along with kinks, corners, and edges, which establish different interactions with reaction intermediates and transition states, yielding specific catalytic activities [11–15]. Besides, catalyst materials are dynamic systems under reaction conditions. Indeed, metal particles change their size, shape, and composition according to the local chemical environment inside the reactor, which dynamically evolves with the proceeding of the reaction [16–18]. Consequently, the amount of the different types of active sites may change during the reaction, which translates into a change in the activity of the catalyst. This complex and dynamic nature of catalyst materials in reaction conditions introduce a "*material gap*" [19], that – if not properly filled – leads to the adoption of catalyst models (e.g., extended surfaces model systems) that may completely miss the actual "*nature*" of the active sites (i.e., the true structure that the catalyst materials adopt under reaction conditions) in the reactor.

Several methods have been reported in the literature to allow for a

* Corresponding author.
E-mail address: matteo.maestri@polimi.it (M. Maestri).

https://doi.org/10.1016/j.cattod.2021.05.016
Received 5 January 2021; Received in revised form 29 April 2021; Accepted 21 May 2021
Available online 6 June 2021

use of first-principles methods even in the presence of "*imperfect theories*". A review of these methods and specific applications is given, for instance, in Ref. [6]. In terms of dealing with the challenge of "*imperfect models*" and describing the "*nature*" of the catalyst in reactive conditions, the modeling of the catalyst structure and its modifications under reaction conditions is needed. In this view, *ab initio* thermodynamics [20] and Wulff-Kaishew construction can be applied for the description of catalyst nanoparticles under reaction conditions. With such methodologies, for example, we performed a predictive analysis of the structural variation of supported $Rh/\alpha\text{-}Al_2O_3$ catalyst nanoparticles as a function of the chemical potential inside a reactor for catalytic partial oxidation (CPO) of methane [18]. In agreement with the experimental evidence, the model described the drastic modifications of the Rh/Al_2O_3 catalyst inside the reactor due to bulk phase transitions and shape modification of the nanoparticles at high coverage of adsorbates. In the case of catalyst samples made of nanoclusters [21–23] or nanoparticles with very small size (lower than a few nanometers) [24], the presence of metastable nanoparticle structures in equilibrium with the thermodynamically stable particle shape can have an important effect on the distribution of the active sites and on the catalytic activity. In this scenario, the catalyst must be described as an ensemble of particle shapes, using, for instance, Boltzmann statistics [24].

These methods make it possible to model the structure and the composition of the catalyst materials during the reaction and thus revealing the "*nature*" of the active sites (i.e., the description of the whole gamut of active sites of the catalysts at a given operating condition). The knowledge of the *nature* of the active sites is a prerequisite to unravel the "*identity*" of the dominant active sites of the catalyst, i.e., the identification of the sites which determine the kinetics of the macroscopic reaction. In fact, due to the strong dependence of the catalytic activity on the structure, the reaction usually is faster on certain types of active sites. In contrast, other active sites bind reactants and reaction intermediates, but they do not give a significant contribution to the overall reaction rate. In a reaction mechanism, the dominant active sites of the catalyst are the ones that provide the fastest rate for the rate-controlling steps (RCSs) of the reaction, and therefore are responsible of the overall reaction rate. Examples of studies on the reactivity of different active sites of the same catalyst are present in the literature [7, 13,15]. The comparison between the sites is usually made in terms of rate per active site and at fixed reaction conditions. However, also the "*nature*" of the catalyst (i.e., the abundance of the different active sites) can play a role in determining their contribution to the overall reaction rate. As result, the "*identity*" of the dominant active sites and the RCSs can change with the reaction conditions in response to structural changes of the catalyst shape and morphology at the different local conditions of chemical potentials at the catalyst surface in the reactor. Thus, proper methodologies able to describe in a self-consistent manner both *nature* and the *identity* of the active sites are required.

In this paper, we introduce a novel methodology for the structure-dependent microkinetic analysis of catalytic systems for the identification of the *nature* and the *identity* of active sites in reaction conditions. The methodology is based on a structure-dependent microkinetic model, i.e., a model that comprises the information of the catalyst structure and activity, and how they change according to the local reaction conditions. The morphology of heterogeneous catalyst nanoparticles as a function of the gas chemical potential is determined by means of *ab initio* thermodynamics and Wulff-Kaishew construction methods. The reaction rates are then calculated by the integration in time of a microkinetic model which describes the catalytic activity of the crystal facets exposed by the catalyst in reaction conditions. The method is applied for the investigation of the direct and reverse water-gas shift (WGS) reacting systems on a 4% $Rh/\alpha\text{-}Al_2O_3$ kinetic experimental campaign published by Donazzi et al. [25,26]. Our structure-dependent microkinetic analysis makes it possible to rationalize that far from equilibrium the two different reacting systems not only follow different reaction pathways in agreement with the experimental evidence but also unveil that the dominant active sites are different for WGS and reverse WGS.

2. Methods

2.1. Electronic structure calculations

Electronic-structure density functional theory (DFT) calculations are performed using the Quantum Espresso [27] suite of codes, with GGA-PBE [28] ultrasoft pseudopotentials and a plane wave basis set. The plane wave and electronic density cut-off energies are set to 476 eV and 3809 eV, respectively. A Monkhorst-Pack of $12 \times 12 \times 12$ k-points sampling is applied for bulk Rh and a proportional grid is used to map the Brillouin zone for the surface slabs. The lattice constant of Rh is calculated with the Birch-Murnaghan equation of state, obtaining a value of 3.83 Å, in agreement with the experimental value (3.80 Å [29]). Periodic slabs with a height taller than 10 Å are employed to represent the catalyst surfaces. A vacuum of 12 Å in the z-direction is introduced between periodic slabs. All the atoms with coordination numbers lower than 12 are allowed to relax. A cubic cell with a side length of 12 Å is chosen for gas-phase calculations. For relax calculations, the convergence forces threshold selected is $2.6\ 10^{-2}$ eV/Å, and a difference in energy lower than $1.36\ 10^{-3}$ eV between two consecutive self-consistent field (SCF) steps is required for convergence. The climbing-image nudged elastic band (CI-NEB) method is used to identify the transition states of the elementary steps, with a 10 images path sampling and a final forces convergence threshold of 0.05 eV/Å. Vibration analyses are performed with the finite-differences method, as implemented in the Atomic Simulation Environment (ASE) library [30]. For normal frequencies evaluation, a displacement of 0.01 Å is applied to all the atoms allowed to relax in the corresponding electronic-structure calculations. To enforce thermodynamic consistency to the microkinetic model, a correction based on the analysis of the major sources of DFT error has been applied [31]. Such an approach consists of identifying the gas molecules which are responsible for the highest source of errors in the DFT calculations and correct their energy to reproduce gas-phase reaction enthalpies. The procedure is described in the Supplementary Information (Section 2). The resulting energy corrections are -0.35 eV for the CO molecule, +0.15 eV for the CO_2, and +0.40 eV for the O_2. The application of the correction resulted also in a value of the binding energy of CO* on the top sites of the Rh(111) facet (-1.54 eV) in good agreement with the experimental value (-1.45 eV) [32]. Without the correction, PBE is known to severely overestimate the CO* adsorption strength on the Rh(111) facet (-1.89 eV).

2.2. Structure-dependent microkinetic model

The structure-dependent microkinetic model is based on *ab initio* thermodynamics, Wulff-Kaishew construction, and harmonic transition state theory (hTST) [33]. It describes the chemistry of CO, H_2O, CO_2, H_2, O_2, and CH_4 interacting with five different crystal facets of Rh, with the Miller index: (100), (110), (111), (311) and (331). The thermodynamic

Table 1
DFT energies at 0 K, enthalpies (H°) and entropies (S°) at 450 °C of the gaseous species included in the structure-dependent microkinetic model.

Molecules	E (0 K) [eV]	S° [eV/K]	H° [eV]
CO_2	−2.889	2.65E-03	−2.577
H_2O	−2.478	2.31E-03	−2.200
H_2	0.000	1.64E-03	0.231
CO	0.000	2.34E-03	0.239
O_2	0.000	2.43E-03	0.241
CH_4	0.484	2.39E-03	0.834

parameters of the gas phase molecules at 450 °C are reported in Table 1.

For each crystal facet, the thermodynamic parameters of 15 reaction intermediates (reported in Table 2) and the kinetic parameters of 23 reversible elementary steps (reported in Table 3) are included to represent the complexity of the possible reaction paths which can develop in the system.

The first 6 elementary steps (R_1 - R_6) describe the adsorption of the gas species. The adsorption of H_2 and CH_4 are dissociative, as those species do not chemically adsorb molecularly on Rh surfaces [34–37]. Reactions R_7 - R_9 describe the reactions of adsorbed H_2O* to give H* and O* species, involving the formation of OH* intermediates. Reactions R_{10} - R_{15} represent the paths that link CO_2** and CO* species, which can be converted via the direct dissociation of CO_2** or via 3 different paths involving carboxyl intermediates. Reactions R_{16} - R_{21} describe the reaction paths of the methanation reaction, in which CO* is reduced to CH_3* via two possible routes: the direct dissociation of CO* or the formation of an OCH* intermediate. The last two elementary steps (R_{22} and R_{23}) describe the formation of HCOO** from CO_2** or OCH*.

The mean-field approximation (MFA) is adopted for the calculation of the reaction rates, which is sufficiently accurate for our analysis. Kinetic Monte Carlo studies are present in the literature [38–40], which show the effects of non-uniform distribution of the reaction intermediates when surface diffusion is limiting. Herein, we chose the MFA because, in our system, the surface diffusion rates are significantly higher than the reaction rates at the temperature investigated. Moreover, the MFA allows for the direct integration of the microkinetic model with the Wulff-Kaishew construction method and the simulation of the gas phase evolution inside the reactor. From the integration of the model in WGS and reverse WGS conditions, we calculated that CO* is the most abundant reaction intermediate (MARI) on all the Rh facets, in agreement with previous calculations [41,42]; therefore, the effect of its binding on the stability of the catalyst facets is accounted for. Moreover, the effect of its coverage is included in the calculation of the enthalpy of reaction intermediates and transition states. For all the other reaction intermediates, the coverages calculated are lower than 0.20; thus, their effect on the catalyst morphology and on the kinetic parameters of the reaction scheme is neglected. The Gibbs free energies of reaction intermediates are calculated within the hindered rotor/hindered translator model [43], whereas the ones of transition states are calculated in the harmonic limit. The surface diffusion of reaction intermediates between the Rh facets is neglected, therefore the model behaves as a "multi-isolated-site".

2.3. Catalyst nanoparticles morphology

The morphology of the catalyst nanoparticles under reaction conditions is determined using *ab initio* thermodynamics and Wulff-Kaishew construction methods. The surface free energies of the Rh crystal facets are calculated accounting for the presence of adsorbed CO* molecules at the surface:

$$\gamma_{(hkl)} = \gamma^{clean}_{(hkl)} + \Gamma_{(hkl)}\vartheta_{CO^*}\left(G_{b,CO^*,(hkl)}(T,\vartheta_{CO^*}) + \Delta\mu_{CO}(T,P_{CO})\right) \quad (1)$$

where $\gamma^{clean}_{(hkl)}$ is the specific surface free energy of the clean facet (hkl), $\Gamma_{(hkl)}$ is its site density in $1/Å^2$ (equal to the inverse of the surface area of the unit cell of the facet), $G_{b,CO^*,(hkl)}$ is the Gibbs binding energy of CO*, which contains a surface concentration term and a lateral interaction energy term that is a function of the CO* coverage (ϑ_{CO^*}). Such a function is calculated from a regression of DFT data obtained at different CO* coverage. Details on the DFT calculated data and the parameters of the model are reported in the Supplementary Information (Section 1).

Once calculated the surface free energies of the catalyst crystal facets, the three-dimensional shape of catalyst nanoparticles under reaction is obtained with the Wulff–Kaishew construction method [44]. The minimum energy for a given volume of a crystal polyhedron is achieved if the distances of its faces from one given point are proportional to their specific surface free energies:

$$h_{(hkl)} = \lambda\,\gamma_{(hkl)} \quad (2)$$

The presence of the support is accounted for by introducing an additional surface in the Wulff-Kaishew construction, which represents the interface between the catalyst and the support, and it is drawn at a distance proportional to the correspondent interface energy. The theoretical studies of García-Mota et al. [45], Marmier et al. [46] and Cheula et al. [18], showed that the hydroxylated α-Al_2O_3 surfaces are stable at high chemical potentials of H_2O ($\Delta\mu_{H_2O} = -1.46$ eV) [18], which corresponds to about 10 atm at 450 °C. Cheula et al. [18] also showed that the interface between Rh(111) and the stoichiometric non-hydroxylated α-Al_2O_3(0001) yields the lowest interface energy. Therefore, in this work, the interface energy between the catalyst and the support is calculated from the analysis of such an interface. Details on the parameters of the model obtained from DFT calculations are reported in the Supplementary Information, Section 1.

From the analysis of the 3D plot of the nanoparticle shape obtained by Wulff-Kaishew construction, we calculate the surface areas (per unit

Table 2
Enthalpies (H°) and entropies (S°) of the reaction intermediates of the structure-dependent microkinetic model, at 450 °C.

Reaction Intermediates	Rh(100)		Rh(110)		Rh(111)		Rh(311)		Rh(331)	
	S° [eV/K]	H° [eV]	S° [eV/K]	H° [eV]	S° [eV/K]	H° [eV]	S° [eV/K]	H° [eV]	S° [eV/K]	H° [eV]
CO_2^{**}	1.43E-03	−2.781	1.14E-03	−3.036	1.22E-03	−2.497	1.30E-03	−3.001	1.27E-03	−3.006
H^*	3.80E-04	−0.435	2.58E-04	−0.295	1.60E-04	−0.407	2.05E-04	−0.400	1.36E-04	−0.458
CO^*	9.49E-04	−1.362	9.73E-04	−1.294	7.93E-04	−1.234	9.80E-04	−1.308	9.57E-04	−1.288
H_2O^*	1.36E-03	−2.440	1.14E-03	−2.543	1.18E-03	−2.392	1.15E-03	−2.619	1.14E-03	−2.600
OH^*	6.53E-04	−2.448	6.92E-04	−2.423	6.31E-04	−2.056	6.24E-04	−2.690	6.80E-04	−2.482
O^*	6.02E-04	−2.081	4.27E-04	−1.967	4.04E-04	−1.934	4.54E-04	−2.092	3.79E-04	−2.126
c $COOH^{**}$	1.29E-03	−3.119	1.41E-03	−3.108	1.29E-03	−2.837	1.35E-03	−3.226	1.43E-03	−3.089
t $COOH^{**}$	1.28E-03	−3.177	1.36E-03	−3.152	1.26E-03	−2.928	1.31E-03	−3.266	1.38E-03	−3.123
$HCOO^{**}$	1.40E-03	−3.040	1.33E-03	−3.479	1.22E-03	−2.963	1.25E-03	−3.595	1.35E-03	−3.455
C^*	3.38E-04	1.012	3.08E-04	1.818	1.86E-04	1.997	3.01E-04	1.564	3.24E-04	1.513
CH^*	5.64E-04	0.859	5.24E-04	1.757	4.51E-04	1.341	4.56E-04	1.321	4.56E-04	1.191
CH_2^*	7.98E-04	1.408	7.97E-04	1.495	6.43E-04	1.484	7.43E-04	1.342	7.30E-04	1.106
CH_3^*	9.50E-04	1.155	9.91E-04	1.135	1.16E-03	1.394	9.10E-04	0.947	8.90E-04	0.741
OCH^{**}	8.60E-04	−1.011	9.70E-04	−0.762	8.60E-04	−0.516	8.60E-04	−1.627	8.80E-04	−1.544

Table 3
Enthalpies (H°) and entropies (S°) of the transition states of the reactions included in the structure-dependent microkinetic model, at 450 °C.

	Transition States										
		Rh(100) S° [eV/K]	Rh(110) H° [eV]	Rh(111) S° [eV/K]	Rh(311) H° [eV]	Rh(331) S° [eV/K]	Rh(100) H° [eV]	Rh(110) S° [eV/K]	Rh(111) H° [eV]	Rh(311) S° [eV/K]	Rh(331) H° [eV]
R_1)	$CO + {}^* \Longleftrightarrow CO^*$	2.34E-03	0.239	2.34E-03	0.239	2.34E-03	0.239	2.34E-03	0.239	2.34E-03	0.239
R_2)	$H_2 + 2\,{}^* \Longleftrightarrow 2\,H^*$	1.64E-03	0.231	1.64E-03	0.231	1.64E-03	0.244	1.64E-03	0.231	1.64E-03	0.254
R_3)	$CO_2 + 2\,{}^* \Longleftrightarrow CO_2^{**}$	1.37E-03	−2.469	2.65E-03	−2.577	1.26E-03	−2.371	2.65E-03	−2.577	2.65E-03	−2.577
R_4)	$H_2O + {}^* \Longleftrightarrow H_2O^*$	2.31E-03	−2.200	2.31E-03	−2.200	2.31E-03	−2.200	2.31E-03	−2.200	2.31E-03	−2.200
R_5)	$CH_4 + 2\,{}^* \Longleftrightarrow CH_3^* + H^*$	1.06E-03	1.326	1.03E-03	1.378	1.10E-03	1.523	1.03E-03	1.222	1.47E-03	0.000
R_6)	$O_2 + 2\,{}^* \Longleftrightarrow 2\,O^*$	2.43E-03	0.241	2.43E-03	0.241	2.43E-03	0.241	2.43E-03	0.241	2.43E-03	0.241
R_7)	$H_2O^* + {}^* \Longleftrightarrow H^* + OH^*$	8.98E-04	−1.993	8.06E-04	−1.983	9.24E-04	−1.704	7.75E-04	−2.008	7.69E-04	−2.003
R_8)	$H_2O^* + O^* \Longleftrightarrow OH^* + OH^*$	1.96E-03	−4.521	1.27E-03	−4.023	1.26E-03	−4.112	1.23E-03	−4.275	1.24E-03	−4.192
R_9)	$OH^* + {}^* \Longleftrightarrow H^* + O^*$	5.77E-04	−1.827	7.12E-04	−1.496	5.55E-04	−1.288	5.86E-04	−1.768	6.10E-04	−1.471
R_{10})	$CO_2^{**} \Longleftrightarrow CO^* + O^*$	1.12E-03	−2.595	1.20E-03	−1.985	1.06E-03	−1.992	1.23E-03	−1.899	1.28E-03	−1.920
R_{11})	$CO_2^{**} + H^* \Longleftrightarrow t\,COOH^{**} + {}^*$	1.39E-03	−2.319	1.38E-03	−2.362	1.28E-03	−2.055	1.32E-03	−2.483	1.36E-03	−2.391
R_{12})	$CO_2^{**} + OH^* \Longleftrightarrow t\,COOH^{**} + O^*$	1.51E-03	−5.049	1.63E-03	−5.063	1.85E-03	−4.554	1.57E-03	−5.193	1.55E-03	−5.152
R_{13})	$CO_2^{**} + H_2O^* \Longleftrightarrow t\,COOH^{**} + OH^*$	2.79E-03	−5.221	1.91E-03	−5.471	2.40E-03	−4.889	2.46E-03	−5.620	2.06E-03	−5.605
R_{14})	$t\,COOH^{**} \Longleftrightarrow c\,COOH^{**}$	1.17E-03	−2.911	1.34E-03	−2.763	1.25E-03	−2.512	1.27E-03	−2.894	1.33E-03	−2.758
R_{15})	$c\,COOH^{**} \Longleftrightarrow CO^* + OH^*$	1.35E-03	−2.654	1.40E-03	−2.747	1.29E-03	−2.465	1.35E-03	−2.828	1.41E-03	−2.714
R_{16})	$CO^* \Longleftrightarrow C^* + O^*$	5.80E-04	0.557	6.23E-04	1.078	4.10E-04	1.587	1.81E-03	1.203	1.76E-03	1.140
R_{17})	$C^* + H^* \Longleftrightarrow CH^* + {}^*$	4.23E-04	1.266	4.60E-04	2.055	2.71E-04	2.168	3.61E-04	1.835	3.35E-04	1.945
R_{18})	$CH^* + H^* \Longleftrightarrow CH_2^* + {}^*$	7.98E-04	1.408	6.51E-04	2.040	6.43E-04	1.484	7.76E-04	1.902	7.00E-04	1.971
R_{19})	$CH_2^* + H^* \Longleftrightarrow CH_3^* + {}^*$	8.84E-04	1.369	8.52E-04	1.412	7.23E-04	1.587	8.77E-04	1.291	9.26E-04	1.351
R_{20})	$CO^* + H^* \Longleftrightarrow OCH^{**}$	9.37E-04	−0.650	9.80E-04	−0.603	7.37E-04	−0.314	1.00E-03	−0.606	1.00E-03	−0.604
R_{21})	$OCH^{**} \Longleftrightarrow CH^* + O^*$	7.70E-04	−0.034	1.05E-03	1.965	6.15E-04	0.849	6.99E-04	2.103	6.45E-04	2.034
R_{22})	$CO_2^{**} + H^* \Longleftrightarrow HCOO^{**} + {}^*$	1.15E-03	−2.663	1.36E-03	−2.508	1.38E-03	−2.013	1.25E-03	−2.507	1.33E-03	−2.465
R_{23})	$OCH^{**} + O^* \Longleftrightarrow HCOO^{**} + {}^*$	1.14E-03	−1.960	1.01E-03	−1.570	9.47E-04	−1.734	1.34E-03	−1.482	1.35E-03	−1.526

of catalyst volume) of the facets of the catalyst, $a_{(hkl)}$. Such quantities identify the relative amount of the different types of active sites provided by the catalyst facets, and they are necessary for the calculation of the reaction rates. At low particle dimensions, size effects resulting from the boundaries between the crystal facets can yield deviations from the Wulff construction model. Moreover, metastable nanoparticle shapes can be present in the catalyst sample [24]. However, in this work, we apply our model for the descriptions of nanoparticle sizes higher than a few nanometers, for which such effects can be reasonably neglected. The Wulff-Kaishew construction is a size-independent method, so it provides a model of the nanoparticles' shape for each given size. As a result, the model has one degree of freedom, i.e., the average nanoparticle diameter, which can be obtained from experimental data, and determines the catalyst dispersion.

2.4. Calculation of reaction rates

The reaction rates of the elementary steps of the reaction scheme are calculated within harmonic transition state theory (h-TST) [33], within the mean-field approximation (MFA):

$$\overrightarrow{r}_j = \frac{k_B T}{h_P} \exp\left(-\frac{G^0_{act,j}}{R_{gas} T}\right) \prod_i (\vartheta_i)^{\overrightarrow{\nu}_{ij}} \tag{3}$$

where $\overrightarrow{r}_j$ (1/s) is the forward reaction rate per active site, k_B is the Boltzmann constant, T is the temperature, h_P is the Planck constant, R_{gas} is the ideal gas constant. $\overrightarrow{\nu}_{ij}$ is an element of the matrix of the stoichiometric coefficient of the reactants, corresponding to species i and elementary step j, and ϑ_i is the coverage of reactant species i. $G^0_{act,j}$ is the Gibbs activation energy, which can be divided into enthalpic ($H^0_{act,j}$) and entropic contributions ($-S^0_{act,j}T$), and it is calculated from the enthalpies and entropies of the transition state (TS) and reactants:

$$G^0_{act,j} = H^0_{act,j} - S^0_{act,j} T = \left(H^0_{TS,j} - S^0_{TS,j} T\right) - \sum_i \overrightarrow{\nu}_{ij} \left(H^0_{i,j} - S^0_{i,j} T\right) \tag{4}$$

where $H^0_{TS,j}$ and $S^0_{TS,j}$ are the enthalpy and the entropy of the TS of elementary step j, and $H^0_{i,j}$ and $S^0_{i,j}$ are the enthalpy and the entropy of reactant species. The superscript "0" specifies that the concentration terms are not included in those enthalpies and entropies, because they are explicitly accounted for in Eq. 3. The arrow over $\overrightarrow{r}_j$ and $\overrightarrow{\nu}_{ij}$ in Eqs. 3 and 4 specify that those variables correspond to the forward direction of the elementary step j, where $\overrightarrow{\nu}_{ij}$ contains only the stoichiometric coefficients of the reactant species. The net reaction rate of the elementary step (r_j) is obtained as $r_j = \overrightarrow{r}_j - \overleftarrow{r}_j$, where $\overleftarrow{r}_j$ is the backward reaction rate calculated with Eqs. 3 and 4, considering only the product species of the elementary step j instead of the reactants.

For the case of non-activated adsorption reactions, the transition state is treated as a free 2D gas, thus obtaining:

$$\overrightarrow{r}_j = \left(\frac{R_{gas} T}{2\pi MW_X}\right)^{0.5} \frac{P_X}{R_{gas} T} (\vartheta_*)^n \frac{1}{\Gamma_{(hkl)}} \tag{5}$$

where MW_X is the molecular weight of the gaseous species X, $\Gamma_{(hkl)}$ is the site density of the facet (in kmol/m^3), n is the number of active sites involved in the adsorption reaction and ϑ_* is the coverage of free active sites.

The effect of the lateral interactions with adsorbed CO* molecules (the MARI at the investigated conditions) are considered in the calculation of the Gibbs free energies of all the reaction intermediates and the transition states. Lateral interaction energy, $\Delta E_{A^*}(\vartheta_{CO^*})$, between the reaction intermediates (A^*) and the CO* molecules are accounted for with regression of DFT calculations data obtained at different CO* coverage. The effect of the CO* coverage on the Gibbs free energy of transition states, instead, is calculated as an average between the lateral interaction energies of the reactants and the products of the corre-

sponding elementary step. Such interaction effects are updated on-the-fly during the integration of the microkinetic model, according to the CO* coverages calculated on the different Rh facets. Details on the parameters of the model calculated from DFT are reported in the Supplementary Information, Section 1.

2.5. Reactor integration

The model is integrated for the description of a steady-state plug-flow reactor (PFR), representative of the annular reactor employed in the experiments of Donazzi et al. [25,26]. We concentrate on the simulation of the chemical kinetics phenomena neglecting mass transfer effects, as the experiments are performed in the kinetic control regime, and they are not affected by mass transfer limitations [25,26]. The governing equations obtained from the mass balance for the PFR rector are:

$$\frac{d\dot{n}_i}{dV} = \frac{1}{\dot{V}}\frac{d\dot{n}_i}{d\tau} = \sum_{(hkl)}^{N_f}\sum_{j}^{N_r} \nu_{ij} R_{j(hkl)} \tag{6}$$

where $\dot{n}_i$ (kmol/s) is the molar flow rate of species i inside the reactor, set to zero for adsorbed species, V (m^3) is the reactor volume, τ is the contact time in the reactor and $\dot{V}$ is the volumetric flow rate. ν_{ij} is the stoichiometric coefficient of the elementary step j for the species i, N_f is the number of crystal facets and N_r is the number of elementary steps in the reaction scheme. $R_{j(hkl)}$ is the net rate of the elementary step j on the facet (hkl), which is calculated as:

$$R_{j(hkl)}\left[\frac{kmol}{m^3 s}\right] = r_{j(hkl)}\left[\frac{1}{s}\right]\alpha_{(hkl)}\left[\frac{m^2}{m^3}\right]\Gamma_{(hkl)}\left[\frac{kmol}{m^2}\right] \tag{7}$$

where $r_{j(hkl)}$ is the net reaction rate per site, calculated as a difference between the forward and the backward reaction rates (obtained with Eqs. 3 and 5). For the case of adsorption/desorption reactions, the net reaction rates per site, $r_{j(hkl)}$, are equal to the turnover frequencies (TOFs). $\alpha_{(hkl)}$ is the specific surface area per unit of reactor volume of the crystal facet (hkl), which is calculated as:

$$\alpha_{(hkl)} = \frac{m_{Rh}}{V_{tot}\rho_{Rh}} a_{(hkl)} \tag{8}$$

where m_{Rh} is the total mass of Rh loaded in the reactor and V_{tot} is the total volume of the reactor. ρ_{Rh} is the density of Rh, $a_{(hkl)}$ is the specific area per unit of catalyst volume of the facet (hkl), calculated with the Wulff-Kaishew construction.

The PFR is integrated using the analogy with a series of CSTRs. The reactor volume is spatially discretized into a number of axially distributed control volumes able to provide a converged solution of the mass balance. These volumes are modeled as steady-state continuously stirred tank reactors (CSTRs). The gas-phase composition in each CSTR is used as the inlet composition of the next one. For each CSTR, the steady-state composition is achieved with the following procedure (reported also in Figure S4 of Supplemental Information):

1) For each crystal facet of the catalyst, the equilibrium coverage of CO* is calculated considering thermodynamic equilibrium between the gas phase and the adsorbed CO* molecules. The value of ϑ_{CO^*} at equilibrium is obtained by minimization of the surface free energy of the facet, $\gamma_{(hkl)}$, with respect to CO* coverage (Eq. 1).
2) The specific surface free energies of the nanoparticle facets are obtained from *ab initio* thermodynamics (Eq. 1), at the calculated CO* coverages. The three-dimensional shape of the catalyst is calculated by Wulff-Kaishew construction (Eq. 2). Then, the specific surface areas of the crystal facets, $\alpha_{(hkl)}$, are calculated (Eq. 8) from the 3D plot.
3) The Gibbs free energies of reaction intermediates and transition states are updated accounting for the calculated CO* coverages on the different catalyst facets, and the kinetic parameters of the microkinetic model change accordingly (Eq. 4).
4) The mass balance of the CSTR is integrated. We obtain at this point the coverages of the reaction intermediates and the rates of production/consumption of the gaseous species.
5) The CO* coverage calculated in the previous step is compared with the one obtained at point 1. If the two values are different, the procedure described from point 2–4 is repeated, until the convergence in the CO* coverage is reached. Then, the gas phase composition is used as inlet composition for the next CSTR-like control volume of the reactor, and the whole procedure is repeated until the length of the reactor is fully characterized.

The methodology is integrated with a home-made library of Python scripts which use tools of Cantera [47] and Pymatgen [48] libraries. During the integration of the structure-dependent microkinetic model, the Gibbs free energies of reaction intermediates and transition states are calculated on-the-fly, from tables of coefficients with the form of the NASA coefficients [49]. Such coefficients are obtained by a regression of Gibbs free energy functions calculated from thermochemistry analysis of DFT calculations.

2.6. Analysis of the microkinetic model

The main reaction pathways that develop at the catalyst surfaces are identified by reaction path analysis (RPA) at a given residence time in the reactor. Among the complete set of reversible elementary steps included in the microkinetic model, the ones which dominate in the consumption of each species are identified, by comparison of their net reaction rates. This allows for the identification of the main reaction paths that the system follows at the desired operative conditions. The derivation of the dominant mechanism by using net consumption rates incorporates both entropic and enthalpic contributions along with the available concentration. Partial equilibrium ratio (φ_j) are calculated, in order to identify which reaction steps are in quasi-equilibrium and which ones are not:

$$\varphi_j = \frac{\overrightarrow{r}_j}{\overrightarrow{r}_j + \overleftarrow{r}_j} \tag{9}$$

where $\overrightarrow{r}_j$ and $\overleftarrow{r}_j$ are the direct and reverse reaction rates of the elementary step j. The partial equilibrium ratio results in a value of 0.5 for pseudo-equilibrated elementary steps.

The rate-controlling steps of the reaction mechanisms are calculated with the method of the degree of rate control (DRC) [48]. The DRC (χ_j) represents the sensitivity of the global reaction rate, R_{tot}, to a variation of the kinetic constants of a reversible elementary step, j, and it is defined as follows:

$$\chi_j = \frac{k_j}{R_{tot}}\left(\frac{\partial R_{tot}}{\partial k_j}\right)_{k_{j'\neq j}, K_j^{eq}} \tag{10}$$

where the partial derivative is calculated holding fixed the kinetic constants of the other elementary steps ($k_{j'\neq j}$) and the equilibrium constant of the step j, K_j^{eq}. To this aim, the kinetic constants of the direct and reverse reaction of step j are multiplied by equal factors, which can be associated with a change in the Gibbs free energy of the transition state of the elementary step.

As demonstrated by Jørgensen et al. [50], the macroscopic reaction orders can be calculated as the sum of the microscopic reaction orders of the elementary steps, weighted by their DRCs:

$$n_X = \frac{\partial \ln(R_{tot})}{\partial \ln(P_X)} = \sum_j^{N_r} \chi_j \frac{\partial \ln(r_j)}{\partial \ln(P_X)} \quad (11)$$

where n_X is the reaction order, and P_X is the partial pressure of species X. As a result, the overall reaction rate results proportional to the product between the elementary steps elevated to their DRCs:

$$R_{tot} \propto \prod_j^{N_r} r_j^{\chi_j} \quad (12)$$

3. Results and discussion

The experimental reaction orders obtained by Donazzi et al. [25,26,51,41] suggest that the two directions of the WGS follow different reaction mechanisms far from equilibrium. The WGS reaction rate shows a first-order dependence with respect to H_2O and a no direct dependence from the amount of CO. The reverse WGS reaction rate results instead proportional to the concentration of CO_2 and independent from the amount of H_2 in the system. Herein, we analyze the two reacting systems with the structure-dependent microkinetic model described in the previous sections, in order to identify the "*identity*" of the dominant active sites and their RCSs, allowing for the interpretation of the macroscopic reaction orders.

3.1. Comparison with experimental data

In order to verify that the model can achieve a quantitative description of the reacting systems, the structure-dependent microkinetic model is integrated to reproduce the experiments of Donazzi et al. [25,26,51,41]. Their experimental setup consists of an annular reactor containing 10 mg of 4% $Rh/\alpha\text{-}Al_2O_3$ catalyst, and the data collected are reactor outlet compositions at different temperatures. The inlet composition for the WGS system is 1.59 % CO, 2.39 % H_2O, in N_2, and the molar flow rate is 1.274 mol/min/g_{cat}. For the reverse WGS, the composition is 1.02 % CO_2, 1.09 % H_2, in N_2, and the molar flow rate is 1.321 mol/min/g_{cat}.

The structure-dependent microkinetic model is based on the Wulff-Kaishew construction, which is a size-independent technique; therefore, it has one degree of freedom, i.e., the nanoparticle diameter. For the sample analyzed, the average nanoparticle diameter is not known beforehand. Hence, we exploit such degree of freedom to best fit the experimental data of reactor outlet composition. By using an average diameter of 6 nm, a good agreement is accomplished between the experiments and the results obtained with the microkinetic model (Tables 1–3). In Fig. 1, the comparison between the model predictions and the experiments is reported.

The fitted value of nanoparticle diameter results in a catalyst dispersion (fraction of Rh atoms exposed to the nanoparticles' surface) of 0.14 Rh_{surf}/Rh_{tot}. The value is reasonably in line with what was reported on similar systems (0.05 Rh_{surf}/Rh_{tot} [51]). Moreover, being the only fitted parameter, the nanoparticle diameter reflects also the different uncertainties and approximations of the model (e.g., DFT functional, reaction rate calculations, etc.). The fitting of the nanoparticle diameter is needed only to get the agreement with the experimental macroscopic reaction rates. The microkinetic analyses shown in the following sections are independent of the nanoparticle diameter, as the Wulff-Kaishew construction is a size-independent method. Thus, the reaction rates are proportional to the surface area of the Rh facets, and their ratio is constant with the nanoparticle size.

3.2. Analysis of WGS and reverse WGS at 450 °C

Now, we focus our analysis on the simulation of WGS and reverse WGS reactions in the annular reactor at the reaction conditions of 450 °C and 1 atm, with a molar flow rate of 0.0314 mol/min/g_{cat}, a stoichiometric concentration of reactants, and a dilution of 0.98 % in N_2. The temperature of 450 °C is selected because the experimental data at this temperature are taken in the kinetic regime (far from the thermodynamic equilibrium). Fig. 2 shows the profiles of the gaseous species partial pressures and the coverages of reaction intermediates as a function of the contact time in the reactor, obtained by integrating the structure-dependent microkinetic model.

The two reaction systems reach the same gas composition at equilibrium, consistently with the thermodynamic equilibrium. The gas-phase partial pressure profiles are also compared with the ones obtained with the structureless microkinetic model of Maestri et al. [51,41], which is trained on a large set of experimental data. The comparison is represented in Figure S1, which shows a very good agreement between the two models.

Once verified that the model can reproduce the macroscopic behavior of the reacting systems, we exploit it to study the "*identity*" of the active site that gives the predominant contribution to the global reaction, accounting for both activity and abundance of the different active sites. The catalytic activity of the different active sites is represented by the turnover frequency (TOFs), i.e., the rates of production (per active site) of the desired product ($r_{j(hkl)}$ in Eq. 7), calculated from the integration of the microkinetic model. The abundance of the

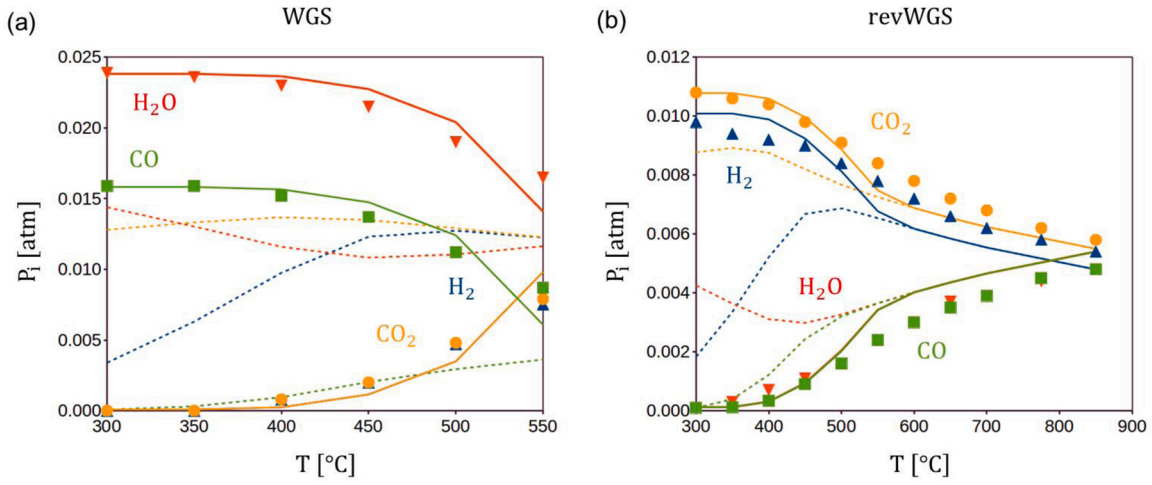

Fig. 1. Molar fractions at the outlet of the annular reactor calculated with the structure-dependent microkinetic model (solid lines) and experimental values of Donazzi et al. (symbols) in (a) WGS conditions (CO, 1.59 %; H_2O, 2.39 %; balance N_2), 0.01274 mol/min and (b) reverse WGS (CO_2, 1.02 %; H_2, 1.09 %; balance N_2), 0.01321 mol/min. With dashed lines are reported the gas phase compositions at the thermodynamic equilibrium.

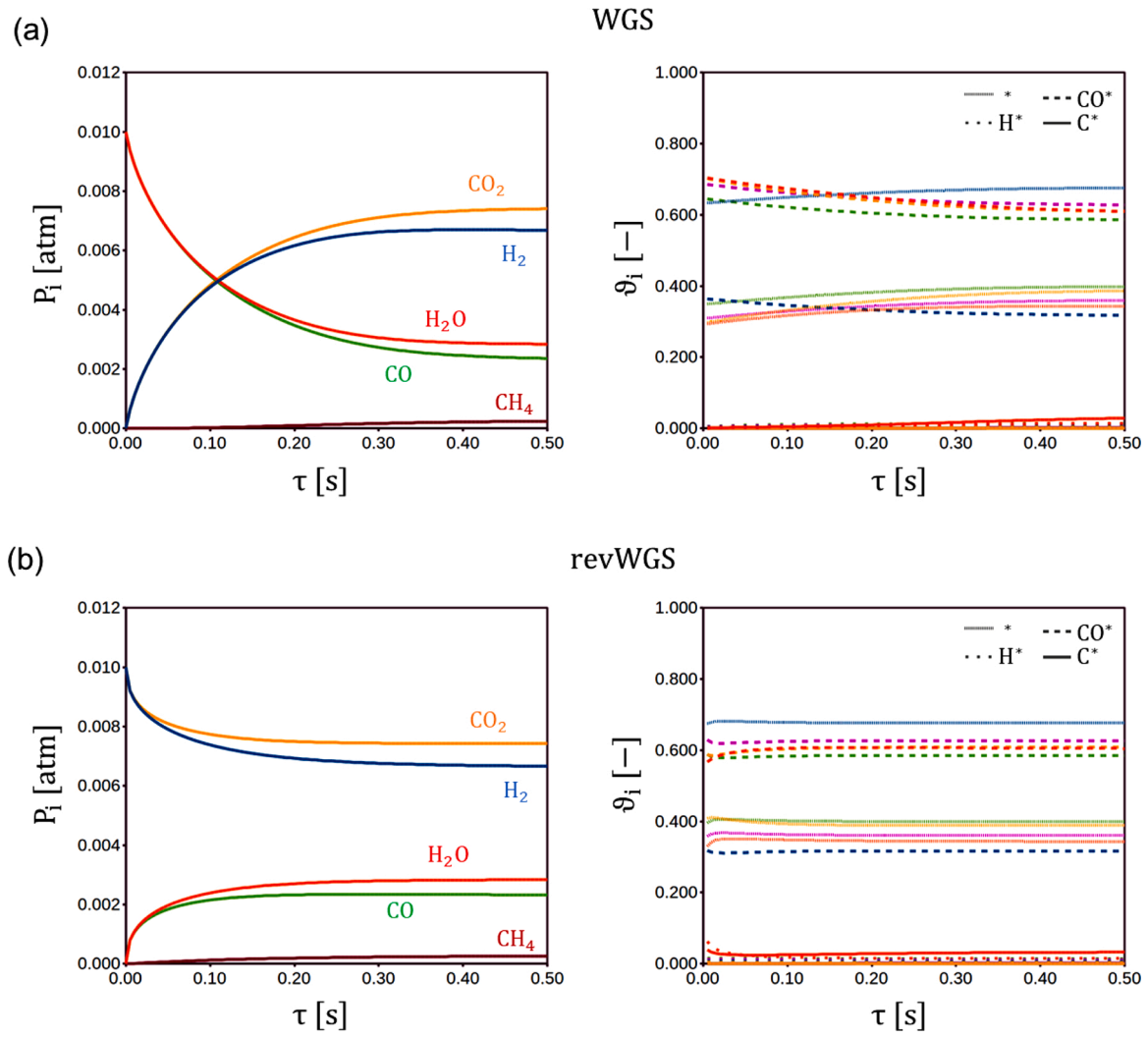

Fig. 2. Profiles of as species partial pressures and as coverages of reaction intermediates as functions of the contact time inside the reactor in WGS (a) and reverse WGS conditions (b), calculated with the structure-dependent microkinetic model. The coverages on the catalyst facets are distinguished with different colors: Rh (100) in red, Rh(110) in orange, Rh(111) in blue, Rh(311) in purple, and Rh(331) in green.

different active sites is represented by the facet areas per unit of reactor volume ($\alpha_{(hkl)}$ in Eq. 7), calculated from the Wulff-Kaishew construction. The combination of activity and abundance yields the productivity of the facets per unit of reactor volume ($R_{j(hkl)}$), calculated from Eq. 7, which represents the contribution to the overall reaction rate provided by the active sites of the different facets. The two systems are analyzed in detail at low contact time (τ) inside the reactor, at which the composition of the gas phase is far from the thermodynamic equilibrium.

During WGS, at $\tau = 10^{-2}$ s, 10 % of CO and H_2O are converted to products ($\eta_{WGS} \cong 2\ 10^{-3}$, where $\eta_R = \left(\prod_i Pi^{\nu_i}\right)/K_{eq,R}$ and $K_{eq,R}$ is the equilibrium constant of the reaction). CO* is the MARI on all the Rh crystal facets, with coverages of 0.70 on Rh(100), 0.71 on Rh(110), 0.38 on Rh(111), 0.70 on (311), and 0.66 on Rh(331). The nanoparticles shape, obtained with the Wulff-Kaishew construction, shows all the Rh facets under investigation (Fig. 3a). The Rh(111) has the widest surface area (38.0 %), followed by Rh(100), with 26.7 %. Then, Rh(110) shows the 15.0 %, Rh(331) the 10.3 % and Rh(311) the 9.8 %.

When we compare the TOFs for the production of H_2 (Fig. 3a), we observe that Rh(311) is the most active Rh crystal facet, showing a turnover frequency (TOF) of 5.8 10^{-1} 1/s. The Rh(111) facet is the second, with a TOF of 2.2 10^{-1} 1/s and Rh(331) is the third most active facet (1.1 10^{-1} 1/s). Less active are Rh(100) (5.9 10^{-2} 1/s) and Rh(110) (3.4 10^{-3} 1/s). When we compare the net production of H_2 of the Rh facets, we discover that despite Rh(111) shows a lower activity per active site than Rh(311), it gives a major contribution to the overall reaction rate (63.9 %). Indeed, Rh(111) produces most of the reaction products due to its higher surface area and density of the active sites. Rh (311) produces only 22.0 % of H_2, followed by Rh(100) (10.2 %) and Rh (331) (3.4 %). The CH_4 production is carried on mainly by Rh(311) (85.5 %), which shows the B_5 active site that is known to be the most active site for CO* dissociation [52].

In reverse WGS conditions at $\tau = 10^{-2}$ s ($\eta_{revWGS} \cong 8\ 10^{-2}$), 11 % of H_2 and CO_2 are converted to CO and H_2O. CO* is the MARI on the Rh facets, with lower coverages (0.50 on Rh(100), 0.52 on Rh(110), 0.24 on Rh(111), 0.57 on Rh(311) and 0.54 on Rh(331)). H* is the second most abundant adsorbate, with coverage lower than 0.10 on all the Rh facets. At the considered reaction conditions, Rh(100) shows the highest TOF for the formation of CO (Fig. 3b). Due to its high catalytic activity, even its surface area is limited (20.38 %), it dominates the reaction mechanism, producing 80.95 % of gaseous CO. Rh(111) and Rh(311) produce 9.86 % and 8.92 % of CO, whereas Rh(110) and Rh(331) give a negligible contribution to the overall reaction rate. The production of CH_4 is carried out mainly by Rh(311) (88.20 %). This analysis points out the importance of accounting for the actual abundance of the active sites of the different crystal facets of the catalyst via structure-dependent microkinetic modeling. Indeed, in WGS reaction conditions, the bare

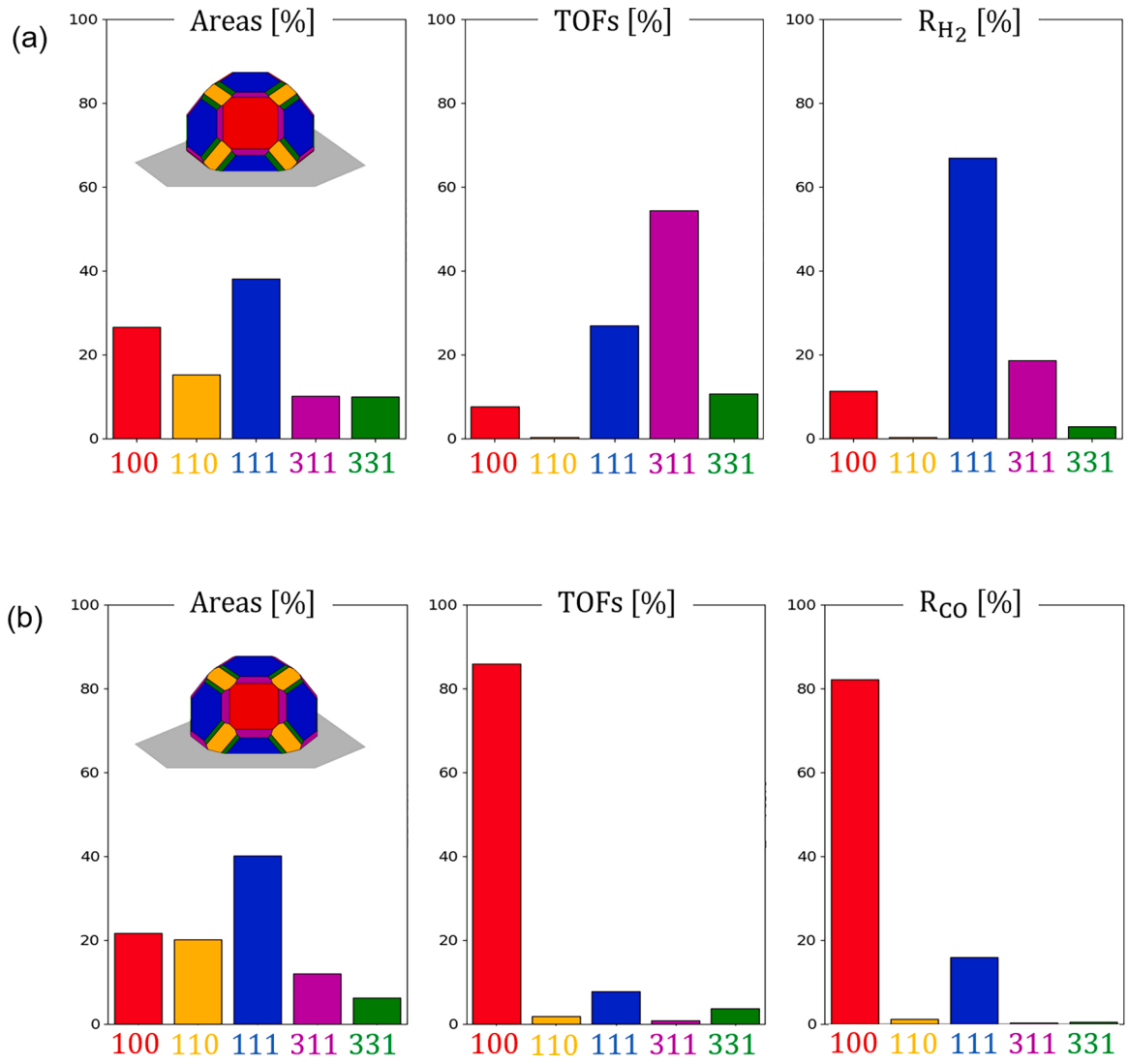

Fig. 3. Catalyst nanoparticles surface areas, turnover frequencies, and production rates for the systems in WGS (a) and reverse WGS (b) conditions out of equilibrium.

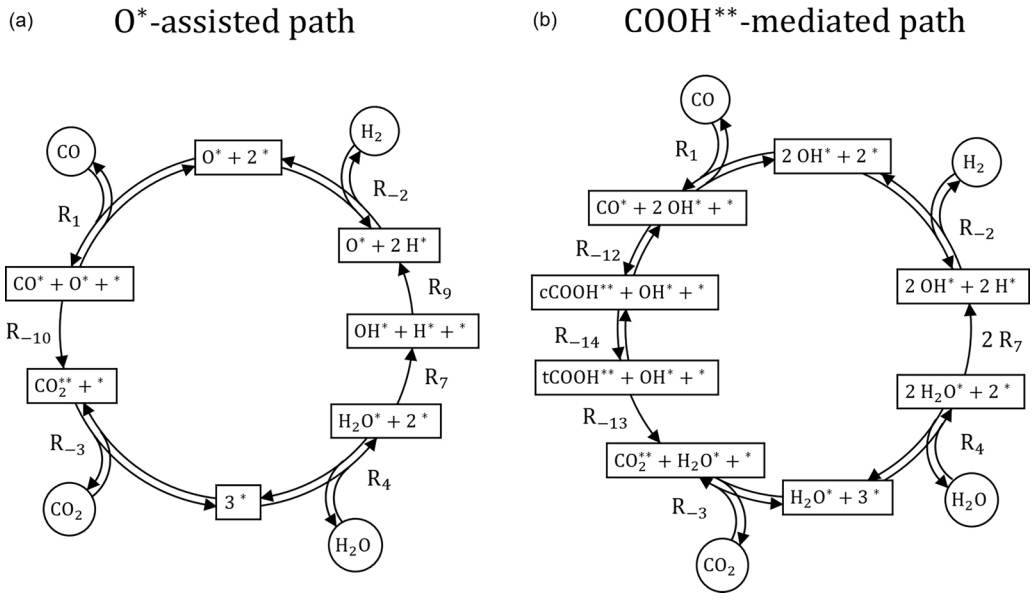

Fig. 4. Two main reaction paths identified for the WGS reacting system. The O*-assisted path (a) involves the direct dissociation of OH* (R_9), which forms O* and H* species. The reverse CO_2** dissociation (R_{-10}) forms CO_2** from CO* and O*. In the COOH**-mediated path (b), OH* reacts with CO* to give c-COOH** (R_{-12}), which isomerizes to t-COOH** (R_{-14}). Then, t-COOH** is converted to CO_2** (R_{-13}), with the formation of an additional H_2O*, which dissociates to give another H* (R_7).

comparison of the TOFs of the crystal facets leads to identify the Rh(311) as the most active facet. However, Rh(111) is the facet that gives the predominant contribution to the overall reaction rate, and such a result is achieved only by calculating the productivities of the facets by multiplying their TOFs with the actual abundance of their active sites.

The WGS reaction system proceeds via two main parallel routes on the Rh crystal facets: oxygen-assisted and carboxyl-mediated pathways, represented in Fig. 4.

In the oxygen-assisted path, OH* species are generated by H_2O* dissociation (R_7) and then dissociate to form O* and H* (R_9). O* then reacts with adsorbed CO* to form CO_2** (R_{-10}). In the carboxyl-mediated path, CO* reacts with OH* species formed through H_2O* dissociation to give a cis carboxylic intermediate, c-COOH** (R_{-15}), which isomerizes to give the trans isomer, t-COOH** (R_{-14}). Then, t-COOH** combines with OH* to form H_2O* and CO_2** adsorbed on the surface (R_{-13}). The plots of the Gibbs free energies of reaction intermediates and transition states for the two main reaction paths at 450 °C are reported in Figs. S2 and S3.

At 450 °C and $\tau = 10^{-2}$ s, on Rh(100) and Rh(110), WGS proceeds almost exclusively via the O*-assisted path. On Rh(111), 58 % of CO_2** is produced by the reaction between CO* and O*, and 41 % from the carboxyl-mediated path. On Rh(311), 67 % of CO_2** is produced from the reaction between t-COOH** and OH*, and 21 % from CO* and O*. On Rh(331), 49 % of CO_2** is produced from CO* and O*, and 24 % from t-COOH** and OH*. Moreover, on this facet, 19 % of CO_2** is produced by an alternative parallel reaction between t-COOH** and O* which form CO_2** and OH* (R_{-11}). On all the crystal facets, the non-equilibrated steps of the main reaction paths are R_7, R_9, R_{-10} and R_{-13} (for Rh(311) also R_{-11}), showing a partial equilibrium ratio higher than 0.90.

The reverse WGS proceeds via two main reaction pathways as well: the H_2O* association and OH* disproportionation paths, represented in Fig. 5.

The H_2O* association path consists of the reversed elementary steps of the oxygen-assisted pathway of WGS. CO_2** dissociates to give CO* and O* (R_{10}). O* species subsequently oxidizes H* to form OH* (R_{-9}). Then, OH* reacts with another H* formed by the dissociative adsorption of H_2 to give H_2O (R_{-7}). The OH* disproportionation path instead involves the reaction between two OH* to give H_2O* and H* (R_8). In this path, the second OH* is produced by an additional reaction between O* and H* (R_{-9}). At 450 °C and $\tau = 10^{-2}$ s, on all the Rh surfaces, reverse WGS reaction proceeds through the H_2O* association path. The OH* disproportionation path becomes relevant at higher temperatures, as reported later in the text. The non-equilibrated steps of the mechanism are R_{-9}, R_{-7} and R_{-10}, showing a partial equilibrium ratio higher than 0.90.

For the WGS system, we find that the DRC of H_2O* dissociation on Rh (111) is the highest ($\chi_{R_{7},(111)} = 0.43$). On the same facet, in decreasing order, we have the DRC of OH* dissociation on Rh(111) ($\chi_{R_{9},(111)} = 0.12$) and the DRC of CO_2** formation ($\chi_{R_{-10},(111)} = 0.08$). On the Rh (311) facet, the DRC of the reaction between t-COOH** and OH* is the highest ($\chi_{R_{-13},(311)} = 0.10$), followed by the one of CO_2** formation ($\chi_{R_{-10},(311)} = 0.08$). Then, on Rh(100), the H_2O* dissociation has the highest DRC ($\chi_{R_{7},(100)} = 0.07$), followed by the OH* dissociation ($\chi_{R_{9},(100)} = 0.04$). The other Rh crystal facets show negligible DRCs in WGS reaction conditions at 450 °C.

For the reverse WGS reaction, we find that the DRC of CO_2** dissociation on Rh(100) is the highest observed ($\chi_{R_{10},(100)} = 0.81$), followed by H_2O* formation on the same facet ($\chi_{R_{-7},(100)} = 0.06$). Other relevant DRCs are the ones of the CO_2** dissociation on Rh(111) ($\chi_{R_{10},(111)} = 0.07$) and CO_2** dissociation on Rh(311) ($\chi_{R_{10},(311)} = 0.04$). The different values for the DRCs of WGS and reverse WGS systems reveal that two directions are characterized by different kinetic relevant steps.

We calculate now the reaction orders of WGS and reverse WGS out of equilibrium from the analysis of the DRCs (Eq. 11), and we compare them with the experiments of Donazzi et al. [25,26]. For the WGS reaction, we calculate with Eq. 12 the proportionality of the overall reaction rate from the microscopic reaction orders of the elementary steps (the full derivation is shown in the Supplementary Information, Section 3), resulting in:

$$R_{tot}^{WGS} \propto \prod_{(hkl)} \left[\left(P_{H_2O}\vartheta_*^2\right)^{\chi_{R_7}} \left(P_{H_2O}P_{H_2}^{-1/2}\vartheta_*^2\right)^{\chi_{R_9}} \left(P_{CO}P_{H_2O}P_{H_2}^{-1}\vartheta_*^2\right)^{\chi_{R_{-10}}} \left(P_{CO}P_{H_2O}^2P_{H_2}^{-1}\vartheta_*^3\right)^{\chi_{R_{-13}}} \right]_{(hkl)} \quad (13)$$

where the fraction of free sites is obtained with the following equation:

$$\vartheta_{*(hkl)} = \frac{1}{1 + K_{eq,CO(hkl)}P_{CO} + K_{eq,H_2(hkl)}P_{H_2}} \quad (14)$$

By introducing the values of the calculated DRCs in Eq. (13), we calculate reaction orders of H_2O and CO equal to 1.12 and -0.61, respectively. The results are in good agreement with the reaction orders observed in the experiments of Donazzi et al. [25,26], which show a direct proportionality of the reaction rate to the partial pressure of H_2O and no direct dependence with respect to CO. As reported above, the H_2O* dissociation is the most relevant elementary step – especially on Rh(111) – showing the highest DRCs ($\sum \chi_{R_7} = 0.52$). This step shows a first-order dependence with respect to the partial pressure of H_2O, along with OH* dissociation ($\sum \chi_{R_9} = 0.17$) and CO_2** formation ($\sum \chi_{R_{-10}} = 0.16$), and this explains the experimental H_2O reaction order. The reaction between t-COOH** and OH*, ($\sum \chi_{R_{-13}} = 0.10$), which is the most relevant step on Rh(311), is instead proportional to $P_{H_2O}^2$. This confirms the fact that such facet is not dominating the overall reaction rate, otherwise, we would have observed a higher H_2O reaction order (closer to 2). The negative order of CO is attributed to its competitive adsorption at the catalyst surface, which results in the blocking of the active sites. This negative proportionality from the amount of CO was not reported by the experimental analysis of Donazzi et al. [25,26]. However, their analysis was carried out including data taken at higher temperatures than 450 °C, at which the CO adsorption can be disfavored. By analyzing the data of Donazzi taken at 450 °C, we calculated a CO reaction order of -0.49 (shown in the Supplementary Information, Section 4), in good agreement with our microkinetic analysis..

In analogy, for the reverse WGS, the proportionality of the overall reaction rate results:

$$R_{tot}^{revWGS} \propto \prod_{(hkl)} \left[\left(P_{CO_2}\vartheta_*^2\right)^{\chi_{R_{10}}} \left(P_{CO_2}P_{H_2}P_{CO}^{-1}\vartheta_*^2\right)^{\chi_{R_{-7}}} \left(P_{CO_2}^2P_{H_2}P_{CO}^{-2}\vartheta_*^2\right)^{\chi_{R_8}} \right]_{(hkl)} \quad (15)$$

For this system, we calculate reaction orders of CO_2 and H_2 equal to 1.01 and 0.11, respectively. As well for the reverse WGS reaction, the DRC analysis is in agreement with reaction orders observed in experiments [25,26], which showed that the overall reaction rate is proportional to the partial pressure of CO_2 and independent from the concentration of H_2. As reported previously, the CO_2** dissociation is the most relevant elementary step – especially on Rh(100) – showing the highest DRCs ($\sum \chi_{R_{10}} = 0.92$). The first order with respect to the partial pressure of CO_2 raises mainly because of its relevance in the kinetic mechanism. The mild positive order of H_2 is attributed to the direct proportionality of H_2O* formation ($\sum \chi_{R_{-7}} = 0.06$) and H_2O* disproportionation ($\sum \chi_{R_8} = 0.01$) reactions. However, their effect is limited because of their small DRCs on all the Rh crystal facets. All in all, this comparison is very encouraging, and these findings call for the performance of a thorough experimental campaign in differential reactor to allow for a detailed comparison between model and experiments in a wide range of operating conditions.

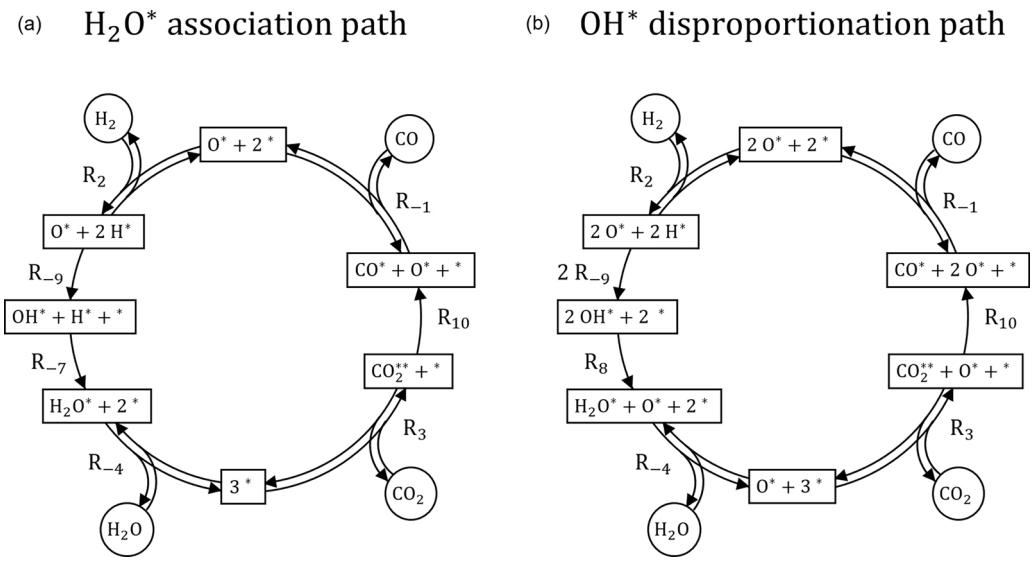

Fig. 5. The main reaction path identified for the reverse WGS reacting system. In the H_2O^* association path (a), H_2O^* is formed from the reaction between OH^* and H^* (R_{-7}). The OH^* disproportionation path (b) instead involves the reaction between two OH^* to give H_2O^* and H^* (R_8). In this path, the second OH^* is produced by an additional reaction between O^* and H^* (R_{-9}).

3.3. *WGS and reverse WGS approaching the thermodynamic equilibrium composition*

After analyzing WGS and reverse WGS far from equilibrium, we study the two reacting systems approaching the thermodynamic equilibrium composition. We express this in terms of the non-equilibrium coefficient of the reverse WGS (η^{revWGS}), defined as:

$$\eta^{revWGS} = \frac{P_{CO}P_{H_2O}}{P_{CO_2}P_{H_2}} \frac{1}{K_{eq}^{revWGS}} \tag{16}$$

where K_{eq}^{revWGS} is equal to $(P_{CO}P_{H_2O})/(P_{CO_2}P_{H_2})$ at thermodynamic equilibrium. As a result, $\log_{10}(\eta^{revWGS})$ shows positive values under WGS conditions, and negative values when reverse WGS is occurring.

In Fig. 6 are reported the DRCs of the most relevant elementary steps of WGS and reverse WGS reactions as a function of $\log_{10}(\eta^{revWGS})$. In this analysis are not considered the steps of the methanation path. Far from equilibrium, the DRCs of the two systems are different, and so is the contribution of the different crystal facets to the reaction rate. During WGS far from equilibrium ($\log_{10}(\eta^{revWGS}) \rangle 1$), Rh(111) gives the highest contribution to the overall rate, and the H_2O^* dissociation on its active sites shows the highest DRC. When WGS approaches equilibrium ($0 < \log_{10}(\eta^{revWGS}) \langle 1$), CO_2^{**} dissociation on Rh(111) and Rh(100) raise their DRCs, evidencing a modification in the reaction mechanism. During reverse WGS far from equilibrium ($\log_{10}(\eta^{revWGS}) \langle -1$), Rh(100) dominates the production of CO and H_2O, and the RCS on such facet is the CO_2^{**} dissociation. When reverse WGS approaches equilibrium

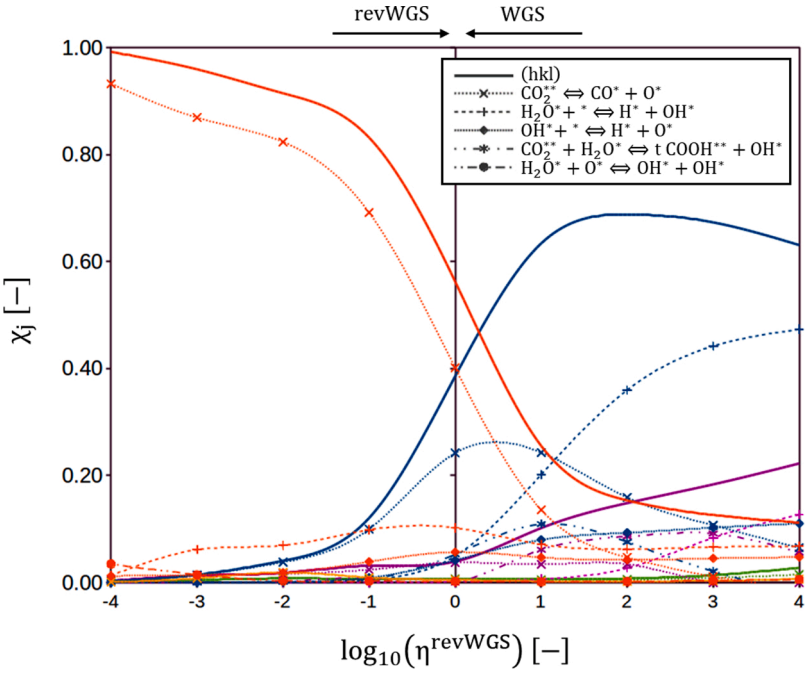

Fig. 6. DRC of the kinetically relevant elementary steps of the reaction (shown in the legend) as a function of the logarithm of the non-equilibrium coefficient of the reverse WGS reaction. The sum of the DRC for each catalyst facet is also represented. The catalyst facets are distinguished with different colors: Rh(100) in red, Rh (110) in orange, Rh(111) in blue, Rh(311) in purple, and Rh(331) in green.

$(-1 < \log_{10}(\eta^{revWGS}) < 0)$, CO_2** dissociation on Rh(111) becomes more kinetically relevant. The different reaction mechanisms and RCSs observed for conditions far from equilibrium does not violate the principle of microscopic reversibility. Indeed, in the systems out of equilibrium, the reaction intermediates have different concentrations (ϑ_i), due to the non-equilibrium conditions, and therefore the reaction rates of the elementary steps are not the same (Eqs. 3 and 5), and this can result in different reaction mechanisms [53]. As the two systems converge to the equilibrium composition of the gas phase ($\log_{10}(\eta^{revWGS}) \rightarrow 0$), the relative amount of the catalyst crystal facets, and their coverages reach the same values. In these conditions, on the basis of the principle of microscopic reversibility, both WGS and reverse WGS follow the same reaction paths (in the opposite directions), with the same RCSs. Indeed, as shown in Fig. 6, the DRCs of the direct and reverse WGS converge to identical values when η^{revWGS} approaches 1.

3.4. WGS and reverse WGS at different temperatures

Now we analyze how the catalytic cycles change with the temperature during WGS and reverse WGS. The atomic species concentration is maintained equal to the one of the previous analysis. At each considered temperature, the systems are analyzed at compositions far from the equilibrium ($\eta_R < 10^{-2}$). The results are reported in Fig. 7.

During WGS, at low temperature, Rh(311) is the dominant catalyst facet, and the reaction proceeds via the carboxyl-mediated path. Between 375 °C and 475 °C, Rh(111) produces most of the reaction products. On such a facet, the COOH**-mediated path is preferred at low temperature, whereas the O*-assisted path is faster at high temperature. Above 475 °C, Rh(100) dominates the WGS reaction, which proceeds via the O*-assisted path. For the reverse WGS, we observe that Rh(111) provides the highest reaction rate at low temperature (below 375 °C), whereas Rh(100) is the dominant catalyst facet at all the other investigated temperatures. The H_2O association is the preferred mechanism below 500 °C. Then, the disproportionation path becomes the relevant reaction path. Interestingly, at the threshold temperature of 500 °C, the CO* coverage on Rh(100) becomes lower than 0.30, value at which the lateral interactions with all the reaction intermediates become null. From this last analysis, we can conclude that also the temperature may induce changes in the "*identity*" of the active sites of the catalyst and the corresponding reaction mechanism.

4. Conclusions

We have proposed a methodology to perform a structure-dependent microkinetic analysis of a catalytic process. Our method makes it possible to unveil the "*nature*" and "*identity*" of the active site in a self-consistent manner. *Ab initio* thermodynamics and Wulff-Kaishew construction are applied to calculate the morphology of the catalyst and how it changes during the reaction. A microkinetic model derived from density functional theory calculations is employed to calculate the reaction rates on the active sites of the catalyst crystal facets exposed under reaction conditions. The methodology has been applied to the study of the WGS and reverse WGS reactions on Rh-based catalysts. For both the reaction systems, we found that the contribution of the different active sites to the overall reaction rate changes importantly with the variation of the reaction conditions. Far from equilibrium, the dominant active sites are found to be the Rh(111) facet during WGS, whereas, for the reverse WGS, the Rh(100) is the facet that dominates the reaction rate. Our analysis pointed out that the *identity* of the active site is determined by both its activity (i.e., the TOF) and the abundance of the different active sites of the catalyst. Thus, the description of both morphology and reactivity of the catalyst nanoparticles in reaction conditions is needed for proper structure-dependent microkinetic modeling. In fact, the contribution of the Rh(311) facet to the WGS reaction rate is found to be lower than the one of Rh(111) because of its limited surface area, even if Rh(311) is the facet that provides the highest TOF. The reaction path analysis of the two systems pointed out that WGS and reverse WGS can proceed according to different dominant reaction mechanisms. In particular, in the case of net-adsorption of CO and H_2O, the reacting system can follow an oxygen-assisted or a carboxyl-mediated mechanism. In the case of net-adsorption of CO_2 and H_2, instead, the reacting system proceeds through the CO_2* decomposition to CO* and O*. For the WGS system, the most relevant step is the H_2O* dissociation on Rh(111). For the reverse WGS system, instead, the dissociation of CO_2 on Rh(100) is the rate-controlling step. In agreement with the experimentally observed reaction orders, we observed that different concentrations of reaction intermediate lead to different kinetic relevant steps in the two directions of the WGS reaction, which develop mainly on different Rh crystal facets. When approaching the equilibrium composition, instead, the reaction paths and the rate-determining steps of the two systems converge in agreement with the microscopic reversibility.

As a whole, our work paves the way towards the use of first-principles methods for the interpretation of the experimental evidence

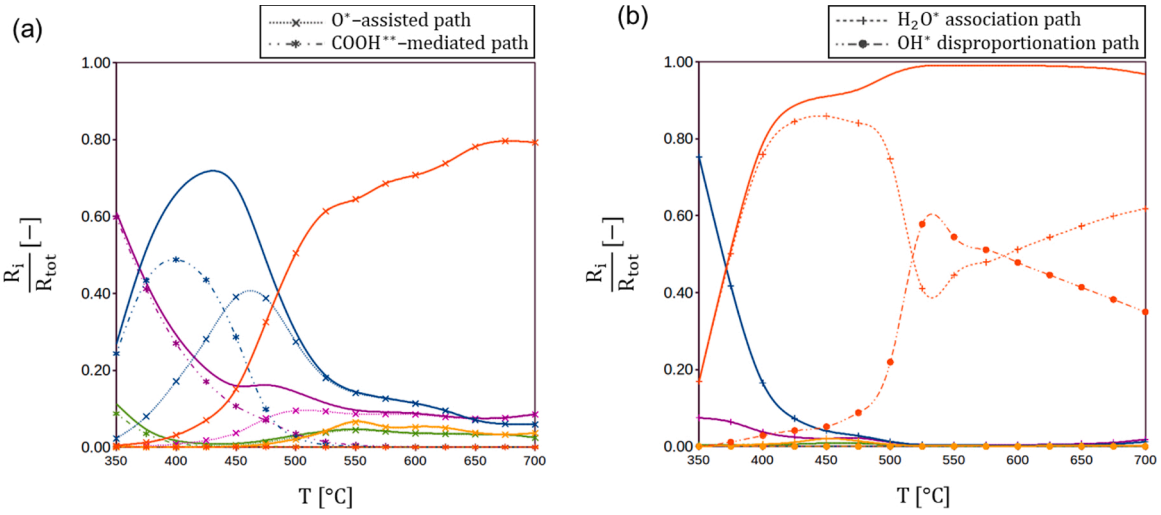

Fig. 7. Trend of productivities and reaction paths (shown in the legend) on the different crystal facets of the Rh catalyst as a function of the temperature, during WGS (a) and reverse WGS (b). The catalyst facets are distinguished with different colors: Rh(100) in red, Rh(110) in orange, Rh(111) in blue, Rh(311) in purple, and Rh (331) in green.

in terms of structure-activity relationships and for the consolidation of fundamental knowledge of an industrial catalytic process at the atomistic scale. Thus, these methods can be considered as an important step forward for the application of fundamental multiscale modeling in catalysis and, in our view, represent the main perspective of multiscale analysis in industrial heterogeneous catalysis for the next years.

CRediT authorship contribution statement

Raffaele Cheula: Investigation, Conceptualization, Formal analysis, Methodology, Visualization, Writing - original draft, Writing - review & editing. **Matteo Maestri:** Supervision, Conceptualization, Formal analysis, Methodology, Writing - original draft, Writing - review & editing, Funding acquisition, Resources, Project administration.

Declaration of Competing Interest

The authors report no declarations of interest.

Acknowledgments

The project leading to this work has received funding from the European Research Council (ERC) under the European Union's Horizon 2020 research and innovation programme (Grant agreement No. 677423/SHAPE: "Structure dependent microkinetic modeling of heterogeneous catalytic processes"). Computational time at CINECA, Bologna (Italy), is gratefully acknowledged.

Appendix A. Supplementary data

Supplementary material related to this article can be found, in the online version, at doi:https://doi.org/10.1016/j.cattod.2021.05.016.

References

[1] A. Bruix, J.T. Margraf, M. Andersen, K. Reuter, First-principles-based multiscale modelling of heterogeneous catalysis, Nat. Catal. 2 (2019) 659–670, https://doi.org/10.1038/s41929-019-0298-3.
[2] M. Salciccioli, M. Stamatakis, S. Caratzoulas, D.G. Vlachos, A review of multiscale modeling of metal-catalyzed reactions: mechanism development for complexity and emergent behavior, Chem. Eng. Sci. 66 (2011) 4319–4355, https://doi.org/10.1016/j.ces.2011.05.050.
[3] M.P. Dudukovic, Frontiers in reactor engineering, Science (80-.) 325 (2009) 698–701, https://doi.org/10.1126/science.1174274.
[4] K. Reuter, H. Metiu, A decade of computational surface catalysis. Handb. Mater. Model., Springer International Publishing, 2020, pp. 1309–1319, https://doi.org/10.1007/978-3-319-44680-6_1.
[5] A.H. Motagamwala, J.A. Dumesic, Microkinetic modeling: a tool for rational catalyst design, Chem. Rev. (2020), https://doi.org/10.1021/acs.chemrev.0c00394.
[6] M. Maestri, Escaping the trap of complication and complexity in multiscale microkinetic modelling of heterogeneous catalytic processes, Chem. Commun. 53 (2017) 10244–10254, https://doi.org/10.1039/c7cc05740g.
[7] M. Jørgensen, H. Grönbeck, First-principles microkinetic modeling of methane oxidation over Pd(100) and Pd(111), ACS Catal. 6 (2016) 6730–6738, https://doi.org/10.1021/acscatal.6b01752.
[8] S. Bhandari, S. Rangarajan, M. Mavrikakis, Combining computational modeling with reaction kinetics experiments for elucidating the in situ nature of the active site in catalysis, Acc. Chem. Res. 53 (2020) 1893–1904, https://doi.org/10.1021/acs.accounts.0c00340.
[9] Y. Wang, H. Wang, A.H. Dam, L. Xiao, Y. Qi, J. Niu, J. Yang, Y.A. Zhu, A. Holmen, D. Chen, Understanding effects of Ni particle size on steam methane reforming activity by combined experimental and theoretical analysis, Catal. Today 355 (2020) 139–147, https://doi.org/10.1016/j.cattod.2019.04.040.
[10] Y. Wang, L. Xiao, Y. Qi, J. Yang, Y.A. Zhu, D. Chen, Insight into size- and metal-dependent activity and the mechanism for steam methane re-forming in nanocatalysis, J. Phys. Chem. C 124 (2020) 2501–2512, https://doi.org/10.1021/acs.jpcc.9b10190.
[11] R.A. Van Santen, Complementary structure sensitive and insensitive catalytic relationships, Acc. Chem. Res. 42 (2009) 57–66, https://doi.org/10.1021/ar800022m.
[12] B. Zijlstra, R.J.P. Broos, W. Chen, G.L. Bezemer, I.A.W. Filot, E.J.M. Hensen, The vital role of step-edge sites for both CO activation and chain growth on cobalt fischer-tropsch catalysts revealed through first-principles-based microkinetic modeling including lateral interactions, ACS Catal. 10 (2020) 9376–9400, https://doi.org/10.1021/acscatal.0c02420.
[13] B. Zijlstra, R.J.P. Broos, W. Chen, I.A.W. Filot, E.J.M. Hensen, First-principles based microkinetic modeling of transient kinetics of CO hydrogenation on cobalt catalysts, Catal. Today 342 (2020) 131–141, https://doi.org/10.1016/j.cattod.2019.03.002.
[14] P. Ghanekar, J. Kubal, Y. Cui, G. Mitchell, W.N. Delgass, F. Ribeiro, J. Greeley, Catalysis at metal/oxide interfaces: density functional theory and microkinetic modeling of water gas shift at Pt/MgO boundaries, Top. Catal. 63 (2020) 673–687, https://doi.org/10.1007/s11244-020-01257-4.
[15] M.M. Kauppinen, M.M. Melander, A.S. Bazhenov, K. Honkala, Unraveling the role of the Rh-ZrO2 interface in the water-gas-shift reaction via a first-principles microkinetic study, ACS Catal. 8 (2018) 11633–11647, https://doi.org/10.1021/acscatal.8b02596.
[16] S. Hannemann, J.D. Grunwaldt, N. van Vegten, A. Baiker, P. Boye, C.G. Schroer, Distinct spatial changes of the catalyst structure inside a fixed-bed microreactor during the partial oxidation of methane over Rh/Al2O3, Catal. Today 126 (2007) 54–63, https://doi.org/10.1016/j.cattod.2006.08.065.
[17] T. Avanesian, S. Dai, M.J. Kale, G.W. Graham, X. Pan, P. Christopher, Quantitative and atomic-scale view of CO-Induced Pt nanoparticle surface reconstruction at saturation coverage via DFT calculations coupled with in situ TEM and IR, J. Am. Chem. Soc. 139 (2017) 4551–4558, https://doi.org/10.1021/jacs.7b01081.
[18] R. Cheula, A. Soon, M. Maestri, Prediction of morphological changes of catalyst materials under reaction conditions by combined: ab initio thermodynamics and microkinetic modelling, Catal. Sci. Technol. 8 (2018) 3493–3503, https://doi.org/10.1039/c8cy00583d.
[19] R. Schlögl, Heterogeneous catalysis, Angew. Chemie - Int. Ed. 54 (2015) 3465–3520, https://doi.org/10.1002/anie.201410738.
[20] J. Rogal, K. Reuter, Ab Initio Atomistic Thermodynamics for Surfaces : A Primer, Notes, 2007, pp. 1–18.
[21] G. Sun, P. Sautet, Metastable structures in cluster catalysis from first-principles: structural ensemble in reaction conditions and metastability triggered reactivity, J. Am. Chem. Soc. 140 (2018) 2812–2820, https://doi.org/10.1021/jacs.7b11239.
[22] E.T. Baxter, M.A. Ha, A.C. Cass, A.N. Alexandrova, S.L. Anderson, Ethylene dehydrogenation on Pt4,7,8 clusters on Al2O3: strong cluster size dependence linked to preferred catalyst morphologies, ACS Catal. 7 (2017) 3322–3335, https://doi.org/10.1021/acscatal.7b00409.
[23] Z. Zhang, B. Zandkarimi, A.N. Alexandrova, Ensembles of metastable states govern heterogeneous catalysis on dynamic interfaces, Acc. Chem. Res. 53 (2020) 447–458, https://doi.org/10.1021/acs.accounts.9b00531.
[24] R. Cheula, M. Maestri, G. Mpourmpakis, Modeling morphology and catalytic activity of nanoparticle ensembles under reaction conditions, ACS Catal. 10 (2020) 6149–6158, https://doi.org/10.1021/acscatal.0c01005.
[25] A. Donazzi, A. Beretta, G. Groppi, P. Forzatti, Catalytic partial oxidation of methane over a 4% Rh/α-Al2O3 catalyst part II: role of CO2 reforming, J. Catal. 255 (2008) 259–268, https://doi.org/10.1016/j.jcat.2008.02.010.
[26] A. Donazzi, A. Beretta, G. Groppi, P. Forzatti, Catalytic partial oxidation of methane over a 4% Rh/α-Al2O3 catalyst. Part I: kinetic study in annular reactor, J. Catal. 255 (2008) 241–258, https://doi.org/10.1016/j.jcat.2008.02.009.
[27] P. Giannozzi, S. Baroni, N. Bonini, M. Calandra, R. Car, C. Cavazzoni, D. Ceresoli, G.L. Chiarotti, M. Cococcioni, I. Dabo, A. Dal Corso, S. De Gironcoli, S. Fabris, G. Fratesi, R. Gebauer, U. Gerstmann, C. Gougoussis, A. Kokalj, M. Lazzeri, L. Martin-Samos, N. Marzari, F. Mauri, R. Mazzarello, S. Paolini, A. Pasquarello, L. Paulatto, C. Sbraccia, S. Scandolo, G. Sclauzero, A.P. Seitsonen, A. Smogunov, P. Umari, R.M. Wentzcovitch, QUANTUM ESPRESSO: a modular and open-source software project for quantum simulations of materials, J. Phys. Condens. Matter 21 (2009), 395502, https://doi.org/10.1088/0953-8984/21/39/395502.
[28] J.P. Perdew, K. Burke, M. Ernzerhof, Generalized gradient approximation made simple, Phys. Rev. Lett. 77 (1996) 3865–3868, https://doi.org/10.1103/PhysRevLett.77.3865.
[29] P. Villars, L.D. Calvert, Pearson's handbook of crystallographic data for intermetallic phases, Am. Soc. Met. (1986) 3258, https://doi.org/10.1002/crat.2170221117.
[30] A. Hjorth Larsen, J. JØrgen Mortensen, J. Blomqvist, I.E. Castelli, R. Christensen, M. Dułak, J. Friis, M.N. Groves, B. Hammer, C. Hargus, E.D. Hermes, P.C. Jennings, P. Bjerre Jensen, J. Kermode, J.R. Kitchin, E. Leonhard Kolsbjerg, J. Kubal, K. Kaasbjerg, S. Lysgaard, J. Bergmann Maronsson, T. Maxson, T. Olsen, L. Pastewka, A. Peterson, C. Rostgaard, J. SchiØtz, O. Schütt, M. Strange, K. S. Thygesen, T. Vegge, L. Vilhelmsen, M. Walter, Z. Zeng, K.W. Jacobsen, The atomic simulation environment - a Python library for working with atoms, J. Phys. Condens. Matter 29 (2017), https://doi.org/10.1088/1361-648X/aa680e.
[31] R. Christensen, H.A. Hansen, T. Vegge, Identifying systematic DFT errors in catalytic reactions, Catal. Sci. Technol. 5 (2015) 4946–4949, https://doi.org/10.1039/c5cy01332a.
[32] M.J.P. Hopstaken, J.W. Niemantsverdriet, Structure sensitivity in the CO oxidation on rhodium: effect of adsorbate coverages on oxidation kinetics on Rh(100) and Rh (111), J. Chem. Phys. 113 (2000) 5457–5465, https://doi.org/10.1063/1.1289764.
[33] H. Eyeing, The activated complex and the absolute rate of chemical reactions, Chem. Rev. 17 (1935) 65–77, https://doi.org/10.1021/cr60056a006.
[34] G. Pauer, A. Eichler, M. Sock, M.G. Ramsey, F. Netzer, A. Winkler, Identification of new adsorption sites of H and D on rhodium(100), J. Chem. Phys. 119 (2003) 5253–5260, https://doi.org/10.1063/1.1597196.
[35] H.J. Kreuzer, Z. Jun, S.H. Payne, W. Nichtl-Pecher, L. Hammer, K. Müller, Thermal desorption kinetics of hydrogen on rhodium (110), Surf. Sci. 303 (1994) 1–15, https://doi.org/10.1016/0039-6028(94)90614-9.

[36] C.N. Stewart, G. Ehrlich, Dynamics of activated chemisorption: methane on rhodium, J. Chem. Phys. 62 (1975) 4672–4682, https://doi.org/10.1063/1.430415.
[37] B.S. Bunnik, G.J. Kramer, Energetics of methane dissociative adsorption on Rh {111} from DFT calculations, J. Catal. 242 (2006) 309–318, https://doi.org/10.1016/j.jcat.2006.06.015.
[38] M. Stamatakis, Y. Chen, D.G. Vlachos, First-principles-based kinetic Monte Carlo simulation of the structure sensitivity of the water-gas shift reaction on platinum surfaces, J. Phys. Chem. C 115 (2011) 24750–24762, https://doi.org/10.1021/jp2071869.
[39] M. Jørgensen, H. Grönbeck, Scaling relations and kinetic Monte Carlo simulations to bridge the materials gap in heterogeneous catalysis, ACS Catal. 7 (2017) 5054–5061, https://doi.org/10.1021/acscatal.7b01194.
[40] M. Andersen, C.P. Plaisance, K. Reuter, Assessment of mean-field microkinetic models for CO methanation on stepped metal surfaces using accelerated kinetic Monte Carlo, J. Chem. Phys. 147 (2017), https://doi.org/10.1063/1.4989511.
[41] M. Maestri, D. Livio, A. Beretta, G. Groppi, Hierarchical refinement of microkinetic models: assessment of the role of the WGS and r-WGS pathways in CH4 partial oxidation on Rh, Ind. Eng. Chem. Res. 53 (2014) 10914–10928, https://doi.org/10.1021/ie501570b.
[42] M. Maestri, K. Reuter, Molecular-level understanding of WGS and reverse WGS reactions on Rh through hierarchical multiscale approach, Chem. Eng. Sci. 74 (2012) 296–299, https://doi.org/10.1016/j.ces.2012.02.043.
[43] L.H. Sprowl, C.T. Campbell, L. Árnadóttir, Hindered translator and hindered rotor models for adsorbates: partition functions and entropies, J. Phys. Chem. C 120 (2016) 9719–9731, https://doi.org/10.1021/acs.jpcc.5b11616.
[44] P. Müller, R. Kern, Equilibrium nano-shape changes induced by epitaxial stress (generalised Wulf-Kaishew theorem), Surf. Sci. 457 (2000) 229–253, https://doi.org/10.1016/S0039-6028(00)00371-X.
[45] M. García-Mota, M. Rieger, K. Reuter, Ab initio prediction of the equilibrium shape of supported Ag nanoparticles on α-Al2O3(0 0 0 1), J. Catal. 321 (2015) 1–6, https://doi.org/10.1016/j.jcat.2014.10.009.
[46] A. Marmier, S.C. Parker, Ab initio morphology and surface thermodynamics of α-Al2O3, Phys. Rev. B - Condens. Matter Mater. Phys. 69 (2004), 115409, https://doi.org/10.1103/PhysRevB.69.115409.
[47] D. Goodwin, H.K. Moffat, R.L. Speth, Cantera: An Object-oriented Software Toolkit for Chemical Kinetics, Thermodynamics, and Transport Properties, 2017, https://doi.org/10.5281/ZENODO.170284.
[48] S.P. Ong, W.D. Richards, A. Jain, G. Hautier, M. Kocher, S. Cholia, D. Gunter, V. L. Chevrier, K.A. Persson, G. Ceder, Python Materials Genomics (pymatgen): a robust, open-source python library for materials analysis, Comput. Mater. Sci. 68 (2013) 314–319, https://doi.org/10.1016/j.commatsci.2012.10.028.
[49] B. Mcbride, S. Gordon, M. Reno, Coefficients for calculating thermodynamic and transport properties of individual species, Nasa Tech. Mem. 4513 (1993) 98.
[50] M. Jørgensen, H. Grönbeck, Connection between macroscopic kinetic measurables and the degree of rate control, Catal. Sci. Technol. 7 (2017) 4034–4040, https://doi.org/10.1039/c7cy01246b.
[51] M. Maestri, D.G. Vlachos, A. Beretta, G. Groppi, E. Tronconi, A C1 microkinetic model for methane conversion to syngas on Rh/Al2O3, AIChE J. 55 (2009) 993–1008, https://doi.org/10.1002/aic.11767.
[52] M. Mavrikakis, M. Bäumer, H.J. Freund, J.K. Nørskov, Structure sensitivity of CO dissociation on Rh surfaces, Catal. Lett. 81 (2002) 153–156, https://doi.org/10.1023/A:1016560502889.
[53] R.M. Krupka, H. Kaplan, K.J. Laidler, Kinetic consequences of the principle of microscopic reversibility, Trans. Faraday Soc. 62 (1966) 2754–2859, https://doi.org/10.1039/tf9666202754.